Measurements of Sea-State Variations Across Oceanic Fronts Using Laser Profilometry

C. R. McCLAIN

NASA/Goddard Space Flight Center, Greenbelt, MD 20771

N. E. HUANG

NASA/Wallops Flight Center, Wallops Island, VA 23337

P. E. LAVIOLETTE

NORDA, NSTL Station, MS 39529

(Manuscript received 2 July 1981, in final form 21 June 1982)

ABSTRACT

As part of the Grand Banks Experiment in May 1979, airborne laser profilometer measurements of the ocean wave field were made across a large cold-water extrusion situated over the Newfoundland Ridge. The feature is actually an extension of the Labrador Current which is bordered on the west side by the Gulf Stream and on the east side by the North Atlantic Current. Star-shaped flight patterns were flown over the fronts on each side of the cold-water feature. A graphic technique was applied to the apparent wavenumber spectra in order to determine the changes in wave energy, wavelength and direction of propagation of the dominant wind-wave and swell components as they move across the fronts. At the western front, the sea state increased abruptly and the results indicate that wave-current interactions were the most important mechanism for wave modification although boundary-layer effects were present and increased wave breaking was observed. At the eastern front, changes in the swell are compared to theoretical predictions and are in very close agreement.

1. Introduction

Dramatic changes in sea state in the vicinity of major oceanic fronts have been observed by mariners for ages. Early attempts to explain changes in wave properties by Bowden (1948) and Barber (1949) coupled the modification to changes in currents such as what one observes at the mouth of a tidal inlet during ebb and flood phases. Longuet-Higgins and Stewart (1960, 1961, 1964) developed the kinematical and dynamical relationships which govern wave refraction and energy exchange between a shearing current and a gravity wave component in terms of radiation stress. These results indicated that wave components were dispersed by the current in a manner dependent upon the phase speed of that component and its initial angle of encounter with the current. This effect was discussed further by Kenyon (1971) who noted that wave components could be reflected, trapped or transmitted by currents such as the Gulf Stream. Such changes in the wave field were observed by Sugimori (1973) in the Kuroshio and by Hayes (1980) in the Gulf Stream. As an illustration of the importance of wave-current interactions, Huang *et al.* (1972) applied the theoretical results for each wave component to the Pierson-Moskowitz spectrum for the simple conditions of winds directly following and opposed to the currents while assuming that all waves were propagating with the wind. That study indicated that significant changes in the spectrum could occur under realistic conditions.

In addition to wave-current interactions, other mechanisms exist which can cause the surface roughness to change in the vicinity of an ocean front. For instance, abrupt changes in the difference between air temperature (T_a) and sea-surface temperature (T_s) can result in marked enhancement of boundary-layer turbulence and hence a more rapid wave growth as when the wind crosses the front from a region where $T_a - T_s$ is positive to an area where it is negative. Various studies such as those by Jones (1953), Kondo (1975) and Sweet *et al.* (1981) indicate that a complicated feedback between the wind profile and the surface roughness exists. The increased roughness also affects the heat-transfer rate and the vertical wind profile. These effects will be compounded in the presence of an increasingly adverse current, the degree of which has not been addressed in the past. The review article by Charnock (1981) indicated that these processes are far from being understood and that a proper approach to such a study would require detailed measurements of the wave field, sea-surface temperature and the marine boundary layer.

The purpose of the study described in the present

paper was to use such an approach to examine the surface-roughness changes across a frontal structure. The study was made as part of the Grand Banks Experiment and was conducted in May 1979 in the region southeast of Newfoundland, over the Newfoundland Ridge. The full rationale for the Grand Banks Experiment is discussed by LaViolette (1981).

The collection of detailed wave information has always been a difficult problem. For this study, the main technique for providing synoptic data on the wave field was the laser profilometer. Profilometry has been used by Barnett and Wilkerson (1967), Ross *et al.* (1970), Schule *et al.* (1971), McClain *et al.* (1979) and Liu and Ross (1980). In most of these studies, the wave fields were dominated by either swell or wind waves and a single flight track was believed to be sufficient. However, in an ocean frontal region where wind waves and swell can coexist and can be refracted, a single flight track would provide insufficient information for a competent wave study. Indeed, multiple-component seas are the rule in these areas rather than the exception. In studying the waves in such a region, a flight plan should be designed to handle not only multiple-component seas but also wave refraction due to current gradients. A flight plan with these objectives in mind was developed for the present study.

Confronted by the complicated environmental problem of sea-surface-roughness changes across an oceanic front, but restricted by available instrumentation, this proposed field study was designed to provide answers to two questions. First, can a laser profilometer be used to study a wave field with more than one dominant component? If the answer is affirmative, then the second question is whether or not these data can be used to determine the effect of wave-current interactions. Of these two questions, the first one at least has to be answered in principle, because the profilometer has not been used to study complicated sea states before.

2. A graphic method of applying profilometry data to the study of complex sea state

One of the main problems encountered in using line profiles derived from laser profilometer data results from wave components not propagating in the direction of flight. Those components are aliased and appear to have longer wavelengths than are actually present. This distortion of the frequency spectrum is demonstrated empirically by McClain *et al.* (1980) where a homogeneous wave field was profiled from several orientations using a star pattern. It is because of distortion and related processing problems that earlier studies were limited to relatively simple wave fields. However, as we will show, the same effect that causes aliasing can, if the data are properly processed, reveal the direction of the waves. A simple graphic method was the technique used in this study and is described in Section 2b. In order to understand the rationale for this method, certain aspects of profilometer data should be discussed. More detailed analyses of wave measurements from a moving platform are provided by Long (1979) and Kats and Spevak (1980). In the following section, a short narrative summary is given.

a. The properties of the profilometer data

As a first-order approximation, the ocean wave field can be treated as a superposition of many different wave components of different wavenumbers and frequencies which are propagating independently. These components may be further grouped into different wave systems, each having a well-defined direction of propagation and a narrow energy band in either frequency or wavenumber space. Let the wave field be represented by the surface elevation function $\zeta(\mathbf{x}, T)$, and

$$\zeta(\mathbf{x}, T) = \int_{\mathbf{k}} \int_{n} A(\mathbf{k}, n) \exp[i(\mathbf{k}\cdot\mathbf{x} - nt)] d\,\mathbf{k} dn, \quad (2.1)$$

where $\mathbf{x}$ is the position vector, T the time, and $A(\mathbf{k}, n)$ a complex-valued random-amplitude function of wavenumber vector $\mathbf{k}$ and frequency n. Since $\zeta(\mathbf{x}, T)$ is always real,

$$A(\mathbf{k}, n) = A^*(-\mathbf{k}, -n), \quad (2.2)$$

with the asterisk denoting the complex conjugate. In a homogeneous wave field, the amplitude function is related to the power spectrum by

$$\overline{A(\mathbf{k}, n)A^*(\mathbf{k}', n')} = X(\mathbf{k}, n)\delta(\mathbf{k} - \mathbf{k}')\delta(n - n'), \quad (2.3)$$

where $X(\mathbf{k}, n)$ is the wavenumber-frequency spectrum of the wave field and $\delta(\ )$ is the delta-function. The overbar denotes the average. By (2.2),

$$X(\mathbf{k}, n) = X(-\mathbf{k}, -n). \quad (2.4)$$

The complete spectrum given in (2.3) requires a simultaneous spatial and temporal data set which is extremely hard to collect. Most of the available data provide only a partial set of information in which ambiguity and complications are unavoidable.

An integrated spectrum over all frequency gives the wavenumber spectrum

$$\Psi(\mathbf{k}) = \int_{-\infty}^{\infty} X(\mathbf{k}, n) dn, \quad (2.5)$$

where $\Psi(\mathbf{k})$ can be obtained from a set of data collected from distributed points at the same time. Jackson *et al.* (1982) describe one technique. The true direction of the wave propagation is not contained in (2.5). A different integration over all wavenumbers will give a frequency spectrum

$$\phi(n) = \int\int_{-\infty}^{\infty} X(\mathbf{k}, n) d\mathbf{k}, \tag{2.6}$$

which can be obtained from a time series at a fixed point. In (2.6), all the directional properties of the wave field are lost.

When measurements of the ocean surface are made from a moving platform traveling at a constant velocity $\mathbf{v}$, the exact location and time of a point on the surface is given by

$$\left.\begin{aligned} \mathbf{x} &= \mathbf{x}_0 + \mathbf{v}T \\ T &= t_0 + t \end{aligned}\right\}, \tag{2.7}$$

where $\mathbf{x}_0$ is an arbitrary initial point at time t_0. The surface elevation recorded by the moving system (assuming that platform motion is accurately removed) will be

$$\zeta(\mathbf{x}, T) = \int_{\mathbf{k}}\int_{n} A(\mathbf{k}, n) \times \exp\{i[\mathbf{k}\cdot(\mathbf{x}_0 + \mathbf{v}t) - n(t_0 + t)]\} d\mathbf{k}dn. \tag{2.8}$$

The covariance function is

$$\overline{\zeta(\mathbf{x}, T)\zeta(\mathbf{x}', T')} = \int_{\mathbf{k}}\int_{\mathbf{k}'}\int_{n}\int_{n'} \overline{A(\mathbf{k}, n)A^*(\mathbf{k}', n')} \exp\{i[(\mathbf{k} - \mathbf{k}')\cdot\mathbf{x}_0 - (n - n')t_0]\} \exp\{i[(\mathbf{k}\cdot\mathbf{v}t - \mathbf{k}'\cdot\mathbf{v}t') - (nt - n't')]\} d\mathbf{k}d\mathbf{k}'dnd n'. \tag{2.9}$$

By using Eq. (2.3), (2.9) may be written as

$$R[\boldsymbol{\gamma}(\tau), \tau] = \int_{\mathbf{k}}\int_{n} X(\mathbf{k}, n) \exp[i(\mathbf{k}\cdot\boldsymbol{\gamma} - n\tau)] d\mathbf{k}dn, \tag{2.10}$$

where $\tau = t - t'$ and $\boldsymbol{\gamma}(\tau) = \mathbf{v}\tau$. By definition, if $R[\ ]$ were known for all $\boldsymbol{\gamma}$ and τ, the power spectrum of the wave field could be obtained explicitly by the inverse transform

$$X(\mathbf{k}, n) = (2\pi)^{-3} \int_{\boldsymbol{\gamma}}\int_{\tau} R[\boldsymbol{\gamma}(\tau), \tau] \times \exp[-i(\mathbf{k}\cdot\boldsymbol{\gamma} - n\tau)] d\boldsymbol{\gamma}d\tau. \tag{2.11}$$

But in the present case, $R[\ ]$ is known only along the flight track. Therefore, all that can be derived from these limited data are the one-dimensional apparent spectra,

$$\hat{\phi}_l(\hat{n}) = \int\int\int_{-\infty}^{\infty} X(\mathbf{k}, n)\delta(\hat{n} - n + \mathbf{k}\cdot\mathbf{v}) d\mathbf{k}dn, \tag{2.12}$$

$$\hat{\Psi}_l(\hat{k}_l) = \int\int\int_{-\infty}^{\infty} X(\mathbf{k}, n)\delta(\hat{k}_l - \mathbf{k}\cdot\mathbf{e}_l + n/|\mathbf{v}|) d\mathbf{k}dn, \tag{2.13}$$

where $\mathbf{e}_l$ is a unit vector in the direction of $\mathbf{v}$.

Technically, the elevation is recorded as a time series, yet the properties of the data, in most cases, are spatial in nature on account of the high velocity of the platform. The relative weights of the spatial and temporal information are determined by the phase function of the Fourier transformations in (2.10) and (2.11). The phase function of the Fourier transform for any wave component can be written as

$$(\mathbf{k}\cdot\boldsymbol{\gamma} - n\tau) = kv\tau\cos\theta[1 - c/(v\cos\theta)], \tag{2.14}$$

where θ is the angle between $\mathbf{v}$ and $\mathbf{k}$ and the phase speed is

$$c = n/k. \tag{2.15}$$

Using the arguments of the δ functions in (2.13) and (2.14) with (2.15), the apparent frequency $\hat{n}$ and apparent wavenumber $\hat{k}_l$ can be defined as

$$\hat{n} = kv\cos\theta[c/(v\cos\theta) - 1], \tag{2.16}$$

$$\hat{k}_l = k\cos\theta[1 - c/(v\cos\theta)]. \tag{2.17}$$

The relationship between the apparent frequency and wavenumber is

$$\hat{n}/\hat{k}_l = -v. \tag{2.18}$$

The apparent wavenumber is simply the component of the true wavenumber along the flight track with the correction for the wave motion. The apparent frequency is just the sum of the Doppler frequency produced by the horizontal motion of the platform and the wave frequency. In most cases, $v \gg c$ is satisfied. Under this condition, the correction due to the wave motion is usually negligible if $\theta \ll 90°$. When θ approaches 90°, the wave motion will become dominating, and if the wave field is essentially unidirectional, a perfect frequency spectrum will be produced.

Eqs. (2.12) and (2.13) define a projection of the three-dimensional spectrum along a flight track. This effect has been described analytically for wind-wave fields having various angular spreading functions by Hammond and McClain (1980). However, that analysis assumes an instantaneous profile across the wave field and does not consider Doppler effects. Since the correction for direction is different for each wave component, there is no unique exact solution of (2.12) and (2.13) for the true wavenumber-frequency spectrum. The presentation of the apparent wavenumber spectra is aided by using Fig. 2.1. The wavenumber-frequency spectrum $X(\mathbf{k}, n)$ is depicted as a three-dimensional body of variable density centered about the surface defined by the dispersion relation-

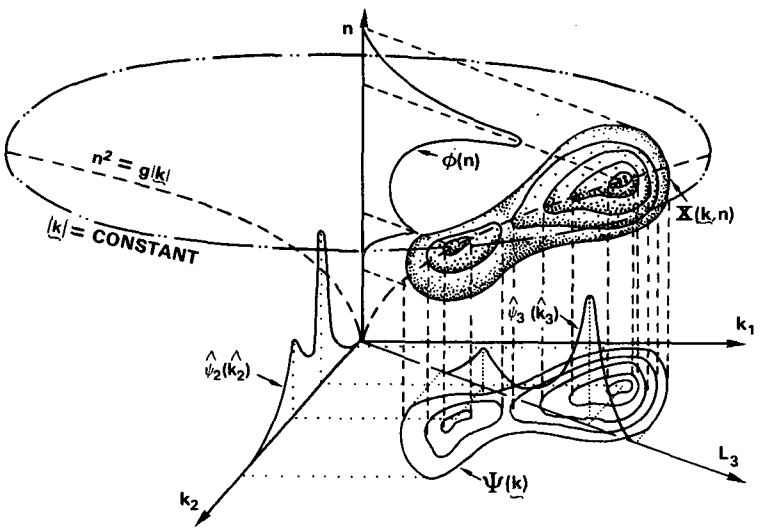

FIG. 2.1. Illustration of the mapping of the directional wave spectra by an airborne profilometer.

ship $n^2 = g|\mathbf{k}|$. The wavenumber spectrum $\Psi(\mathbf{k})$ is related to $X(\mathbf{k}, n)$ by (2.5) and is represented by the contours on the $\mathbf{k}$ plane. The frequency spectrum $\phi(n)$ is derived from $X(\mathbf{k}, n)$ using (2.6). In Fig. 2.1, a two-component wave field is used to illustrate how the peak amplitudes and locations of the apparent wavenumber spectra vary depending on the direction upon which the true wavenumber spectrum is projected. The apparent wavenumber spectrum $\hat{\Psi}_l(\hat{k}_l)$ is defined by (2.13) and $\hat{k}_l$ is determined from (2.17). $\hat{\Psi}_2(\hat{k}_2)$ and $\hat{\Psi}_3(\hat{k}_3)$ are examples. Also, although both the spectral densities and the peak locations are variable, the integrated value under the spectrum, the total energy, is invariant. There is, however, a singular case when

$$\cos\theta - c/v = 0. \tag{2.19}$$

In this situation the profilometer is moving with a component of velocity that is parallel and equal to the phase speed of wave component. A dc signal will result. In a random wave field, this possibility always exists for some components.

It should be reiterated that the apparent wavenumber spectrum is not merely a section of the true spectrum. Rather, it is always a projection of the true spectrum along the flight-track direction in wavenumber space, i.e., the integration of the two-dimensional wavenumber spectrum into an apparent one-dimensional wavenumber spectrum. This integration masks the true information to such a degree that the inversion to retrieve the true two-dimensional spectrum uniquely is, in general, not possible. Special assumptions on the spectral shape can render the problem solvable, but what is easier to do is to determine the true direction of the major wave components by a graphic method discussed in the next section.

b. The graphic method

From the discussion in Section 2a, it is clear that the variations in the energy-peak locations from different flight tracks can be used to determine the directions of the energy-containing components of each wave system. An example can be made of a wave field consisting of two dominant systems each propagating in a different direction, as shown in Fig. 2.2. In this figure, each wave system is represented by a single wave, the wave at the energy peak. The first wave system A is represented by a group of light lines as the wave crests. The wavelength is given by $\overline{OA}$. The second wave system B is represented by a group of heavy lines as the crests and $\overline{OB}$ is the wavelength. When the two wave systems co-exist, the crest lines will form an echelon pattern as shown. In wavenumber space, the wave systems can be represented by two vectors **oa** and **ob** as shown in Fig. 2.3. Since wave system A has a shorter wavelength, it would have a longer wavenumber vector.

As a first approximation, the wave-motion correction can be neglected. An arbitrary flight track Q will see the wave system A as having an apparent wavelength $\overline{OP}$ and wave system B as $\overline{OQ}$. The corresponding apparent wavenumbers are **op** and **oq**. The loci of the terminal points of the apparent wavenumber vectors representing systems A and B are two circles with **oa** and **ob** as the diameters. Although the wave system A has a shorter wavelength than B, the apparent wavelength can be quite different for some flight tracks as discussed before. For example, in flight

track M, the apparent wavelength for system A is longer than B. In wavenumber space, this fact is shown by **om** < **on**. At the intersection points of the crests, the two wave systems will have exactly the same apparent wavelength as at C in Fig. 2.2. The corresponding point in wavenumber space is the intersection point of the two circles. A profilometer flying along $\overline{OC}$ will only see one single wave system. These apparent waves are not free waves, i.e., the wavenumber and frequency do not follow the dispersion relation. In fact, very few of the apparent waves are free. They are purely patterns showing spatial periodicity. By neglecting the wave motion in the first-order approximation, the wave system will be identical whether the waves are propagating in one direction or in the opposite. Therefore, the complete wave pattern could be generated by the mirror images of the wave systems or by the combination of a true wave system and the image of the other. The images of the true waves are represented by dashed circles with the corresponding points indicated by primed letters. When the image of A intersects the true wave system B, or *vice versa*, additional intersecting points are generated at d and d′ in the wavenumber space. The corresponding points in physical space are D and D′.

As discussed in the previous section, the propagation velocity of the waves relative to the motion of the profilometer will produce a second-order correction. The amount of the correction is given by the second term in (2.17). If the wave motion correction is taken into consideration, the circles become cardioids, the solid curves in Fig. 2.4. Even though neither the directions nor the true wavelengths are known *a priori*, the actual data collected will fall on these cardioids. In fact, since the direction θ is undetermined at this point, it is impossible to make a wave-motion correction. After the directions are determined, the shift due to wave motion can be used to resolve the 180° ambiguity in wave-propagation direction. With the first-order apparent wavenumber spectra used as the inputs, the graphic method of determining the wave direction consists of the following steps:

1) Identifying the peak locations in each apparent wavenumber spectrum.

2) Calculating the apparent wavelengths based on the apparent wavenumbers at the peaks.

3) Determining the terminal points of the wavelength along each flight track starting from a common origin.

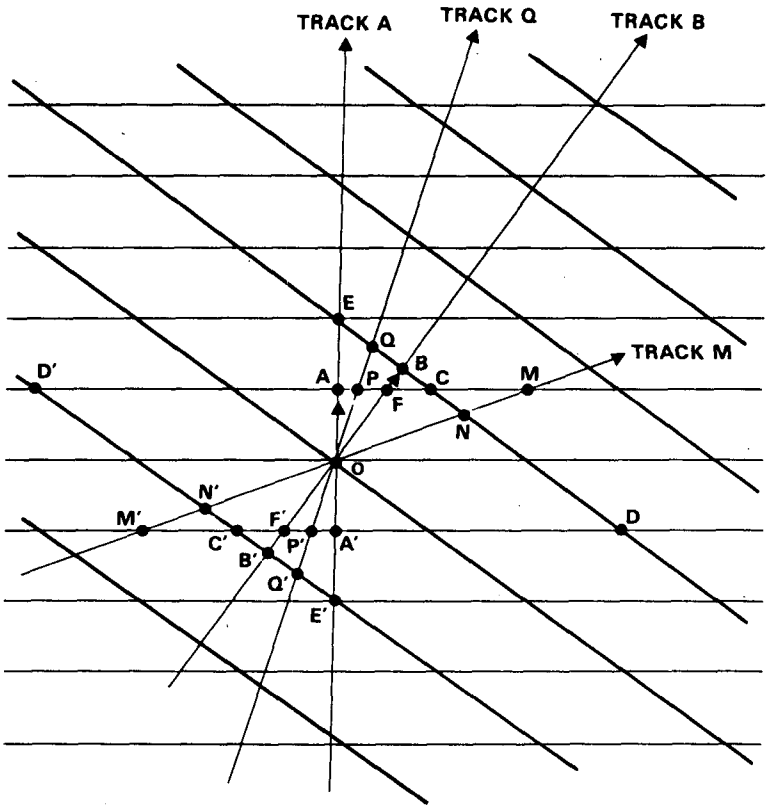

FIG. 2.2. Representation of the mismapping of wavelength by a profilometer for a two-component wave field.

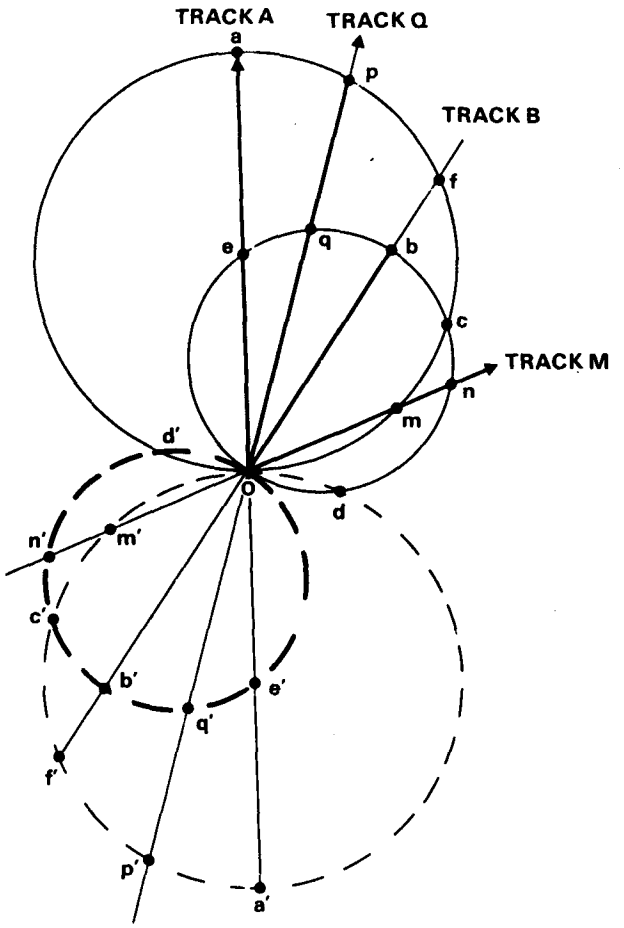

FIG. 2.3. Representation of the mismapping of wavenumber by a profilometer for a two-component wave field.

4) Determining a set of best fitting lines through the terminal points of the wavelength segments.

These best-fitting lines are the crest-lines of wave systems. The normal lines from the crest-lines to the origin give the directions of wave propagation, and the length of these normal lines will be the true wavelengths.

For flight tracks A, B, Q and M the terminal points along each track are (A, E), (F, B), (P, Q) and (N, M) respectively. The best-fitting lines would be $\overline{AM}$ and $\overline{EN}$. The points will not fall exactly on straight lines because of random errors in the observations and wave motion, but the wave motion will give a systematic shift. When the profilometer is flying with (against) the waves, the apparent wavelength will lengthen (shorten) by the factor

$$\hat{\lambda}/\lambda = |v/(v\cos\theta - c)| \qquad (2.20)$$

as shown in Fig. 2.4. This amount of change should be detectable.

3. The experiment and the environmental data

The site for the Grand Banks Experiment was an ocean area southeast of the Tail of the Grand Banks. The area forms what is believed to be the easternmost extent of the main Gulf Stream. Here a major portion of the Gulf Stream goes south, while a secondary portion flows north to become part of the North Atlantic Current (Clarke *et al.*, 1980). Balancing the movement of these warmer currents are, to the north and northwest, the cold waters of the Labrador and Slope Water currents. The confluence of these currents over the Newfoundland Ridge creates large masses of cold water which are constantly being extruded southeast into the warmer waters (LaViolette *et al.*, 1980; LaViolette, 1981). The surface manifestations of these extrusions appear in the infrared imagery as sharp, well-defined frontal features that are directly related to subsurface structure that extends as deep as 1500 m.

Monitoring the surface movement of the extrusions with satellite imagery is hampered by the ex-

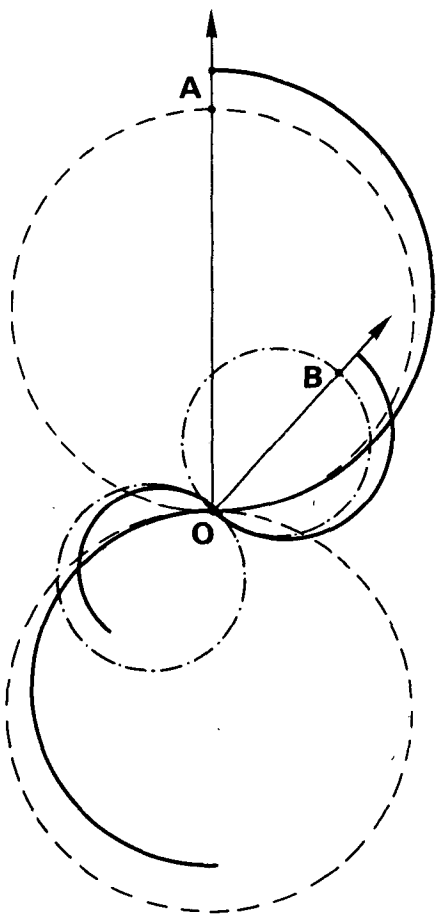

FIG. 2.4. The effects of wave motion on the apparent wavenumber.

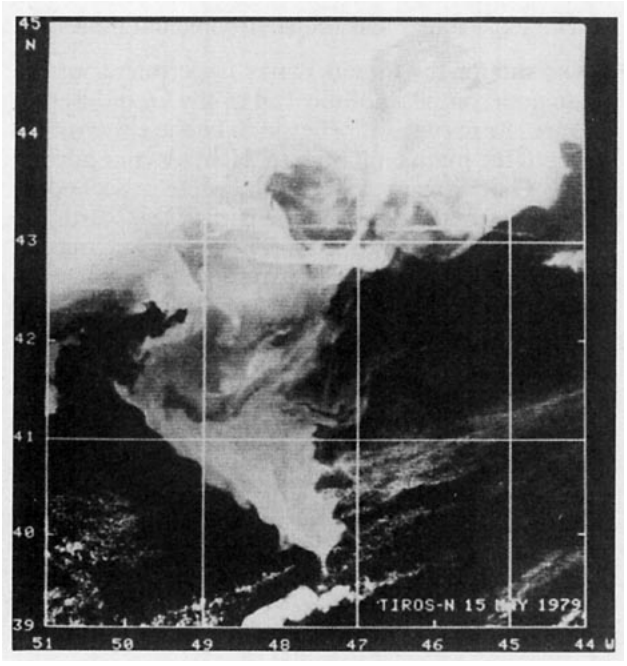

FIG. 3.1. TIROS-N/AVHRR image of the Grand Banks, 15 May 1979.

tensive regional cloud cover. Since radar images often show what appear to be ocean fronts (Fu and Holt, 1982) and because radars have an all-weather capability, they promise to be a supplemental tool to infrared imagery. This portion of the Grand Banks Experiment was designed to determine what mechanisms cause imaging radars, particularly SEASAT SAR, to be sensitive to ocean fronts.

This phase of the Grand Banks Experiment took place during the period 9–20 May 1979. Fig. 3.1 is an enhanced TIROS-N infrared image of the region taken on 15 May 1979. The cold feature shown in the image is typical of the cold-water extrusions described above. Analysis of airborne radiation temperature (ART) data taken on 9 and 10 May is shown in Fig. 3.2. Note the sharp gradient across the western front. The effect of the SST gradients near the fronts on the atmospheric boundary layer is shown by the PRT-5 and Inertial Navigation System (INS) vertical accelerometer traces (Fig. 3.3). These correspond to the track A-A′ in Fig. 3.2. This striking correlation between SST gradients and atmospheric turbulence was a constant feature of the flights over the front during the survey. On 10 May, the data show that the wind blowing across the front created a slight displacement of the more turbulent air over the cooler water. Over the western front, the wind (derived from the aircraft INS) was from 260° at 10 m s^{-1}. Over the center of the cold feature, the wind vector changed to 8 m s^{-1} at 275°. On the eastern front, this change in the mean wind was more pronounced, 9 m s^{-1} at 300°. While the displacement of the turbulent air

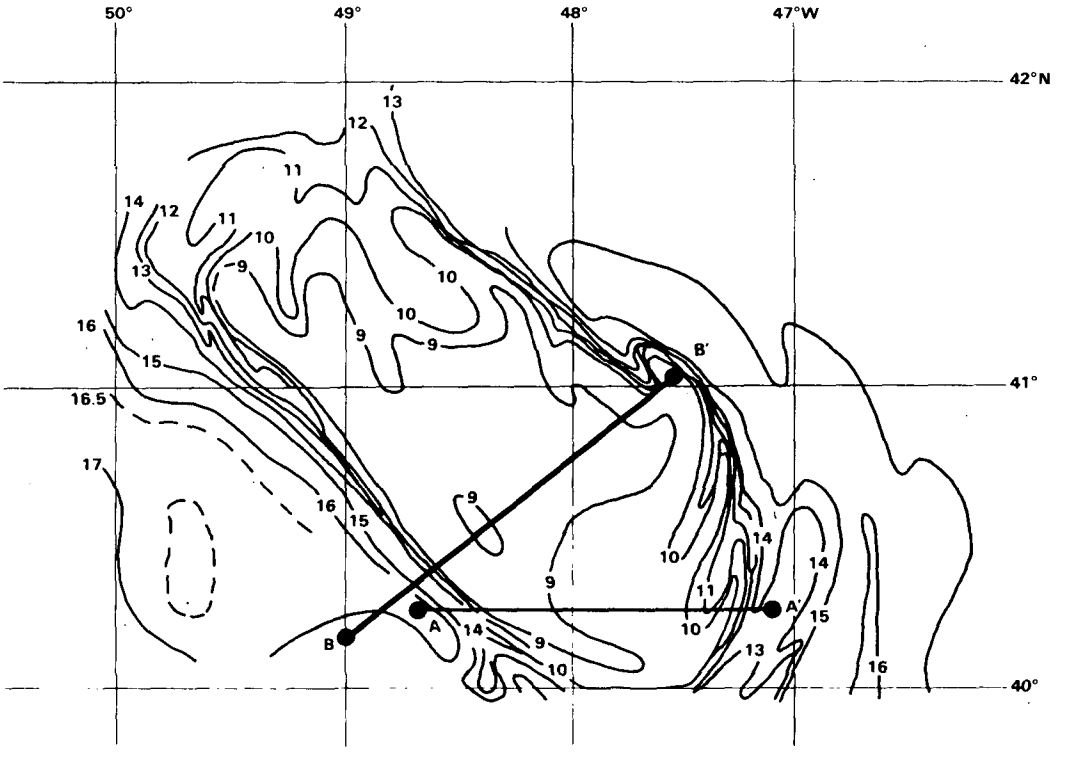

FIG. 3.2. Analysis of aircraft PRT-5 (°C) data collected on 9–10 May 1979.

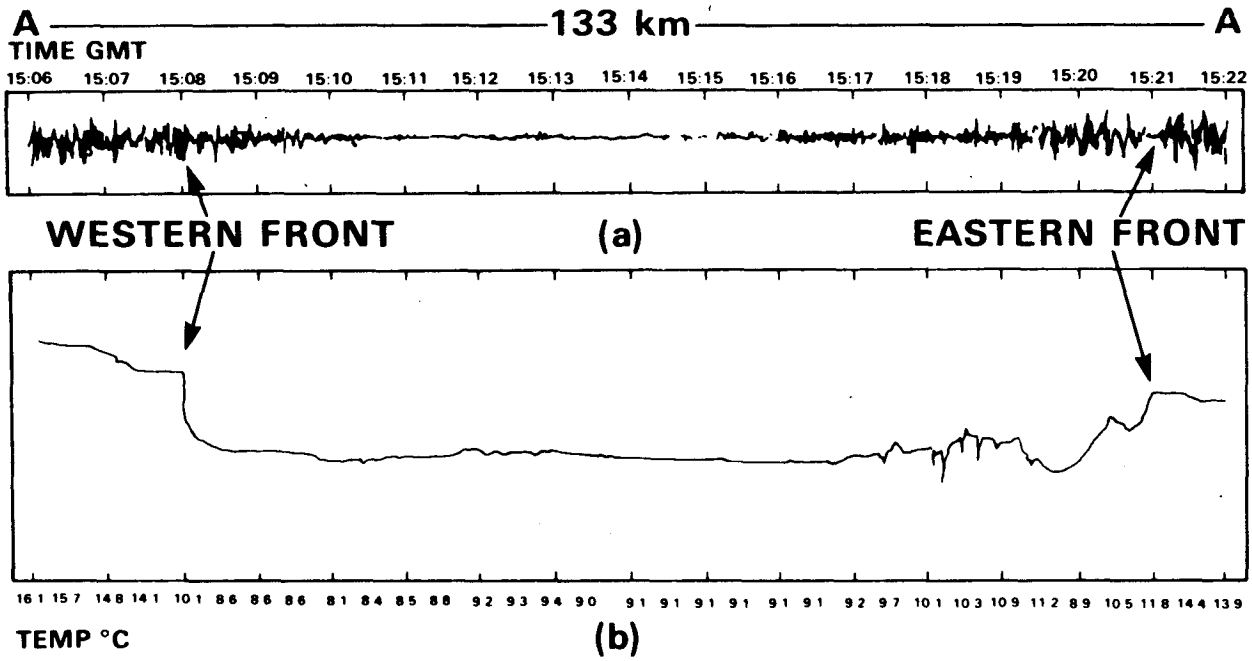

FIG. 3.3. Aircraft-accelerometer (a) and PRT-5 (b) data along flight track A-A', 10 May 1979.

mass was apparent at 250 m, other environmental data indicate that the displacement diminished with altitude until, at the surface, the turbulence coincided with the front. This effect was apparent on all days.

In the original plan of operation, the USNS *Lynch* was to have joined the survey in order to make detailed measurements of the marine boundary layer, the ocean front's thermohaline structure, and the wave and current fields. Unfortunately, a severe storm prevented the ship from entering the area in time to participate in the survey and none of these data were collected. These data would have been invaluable for the study since both mechanisms of wave modification discussed in Section 1 seem to have been at work in the area during the experiment period.

Once the broad regional surveys of the 9th and 10th were complete, detailed aircraft investigations involving right-angle cross-sectional slices across the frontal structure were conducted on the 16th and 17th. The delay between the two series of flights was due to the storm and aircraft problems. The position of these flight tracks for both the 16th and 17th in relation to the overall surface-temperature feature is shown in Fig. 3.2 as line B-B'.

In the absence of the ship, a rather novel approach for measuring the current field was employed. Sonobuoys were dropped at ~9 km intervals along a single track across the entire feature. These sank to a depth of 18 m and presumably drifted with the current. The sonobuoys were twice relocated by the aircraft in an attempt to derive close approximations of the current speed and direction (Fig. 3.4). Unfortunately, on 17 May, a plot of the original drop positions and the two sets of later positions show a systematic displacement that was repeated in all the original drop positions. Analysis of the data indicates a navigation error that is not correctable. Therefore, the initial drop points are not used for the calculation of the current velocity. The second and third sets of sonobuoy locations are used. The time duration between the tracking points for sonobuoy 1 was 2 h and 7 min, whereas the time difference for sonobuoy 15 is only 1 h and 2 min. Comparing the results of this day's data with those for a similar sonobuoy drop on the 16th shows that the results are consistent. The star patterns included in Fig. 3.4b are the flight tracks of the profilometer which will be discussed shortly. In addition to sonobuoys, a finely spaced dye study across the temperature boundary of the western front was conducted on the 16th. The results of these measurements are given in Fig. 3.5. Note that there is a strong shear at the front that is not resolved even by this method. To assist the wave investigation, nadir-looking aerial photographs were taken during the 17th. These proved to be of limited use since the wave field was sufficiently confused as to make it impossible to define clearly the wave field's dominant directions. However, they did show the sudden enhancement of wave-breaking at the western front. The INS winds at 250 m altitude on the 17th were 81° at 12.5 m s^{-1} over the western front and 100° at 8.5 m s^{-1} over the eastern front.

Fig. 3.6 shows the Canadian METOC wave-field analysis for the general area on the 17th with the

study area on the 16th and 17th labeled. The arrows in the wave-field analysis indicate the wave-propagation direction. Those indicating wind waves have the standard wind-speed representation on the tail. The other arrows indicate swell. The convention is period/height (seconds/meters). From Fig. 3.6, there appear to be three wave trains which are the wind-wave field, a swell from the SE, and a swell from the NE. This fact explains some of the difficulty in using the aerial photography. Past experience with this form of wave analysis has been that the $H_{1/3}$ (significant wave height) values are generally reliable, but the periods tend to be low.

Incorporating the requirements for graphic analyses presented in Section 2, the two star patterns flown on the 17th were centered at the maximum temperature gradient. PRT-5 data were recorded simultaneously with vertical-acceleration and laser-profilometer data and were used as a guide in segmenting the data along each track of the pattern. The western pattern is referred to as Star 1 and the eastern pattern as Star 2.

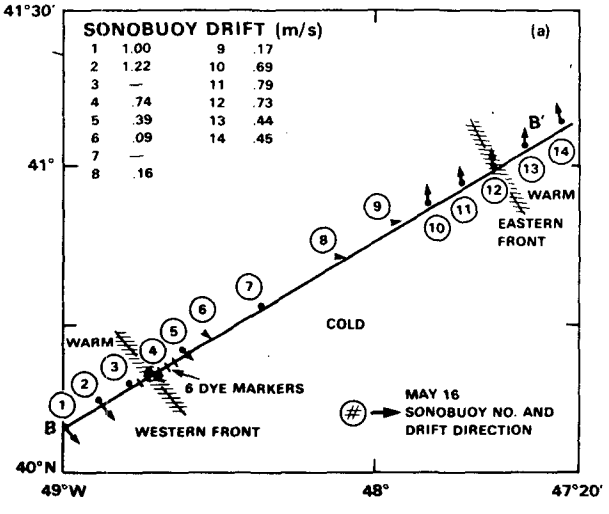

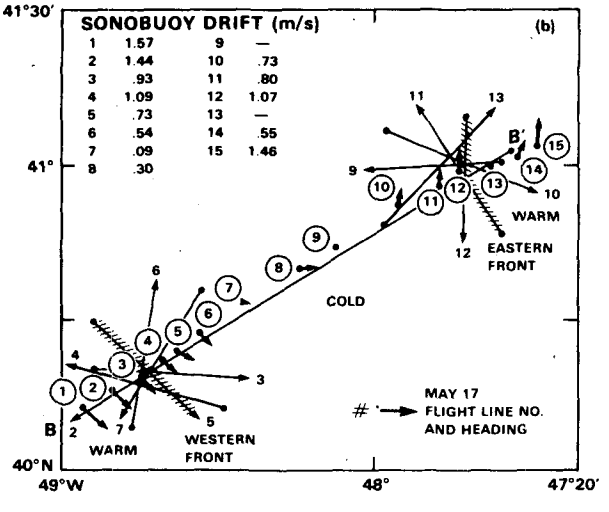

FIG. 3.4. Lagrangian drift measurements on (a) 16 May and (b) 17 May 1979.

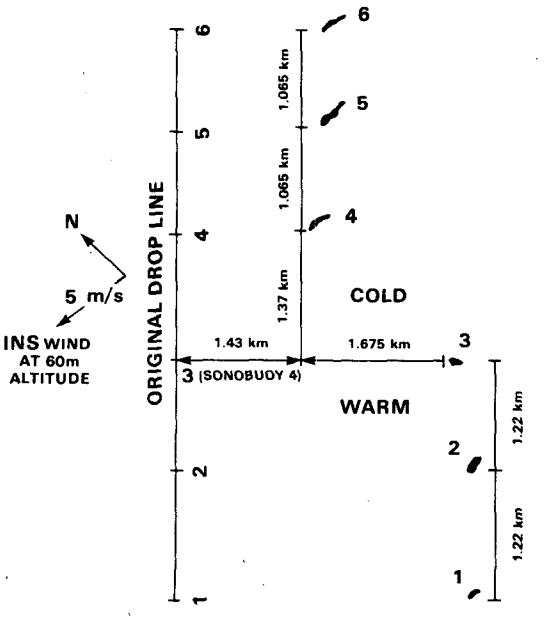

FIG. 3.5. Dye-marker drifts across the western front on 17 May 1979. The elapsed time was 70 min.

4. Processing the profilometer data

One of the most serious problems encountered in processing laser-profilometer data is the removal of vertical aircraft motion. The standard technique to compensate for this motion uses a high-pass filter. This practice is not always adequate. For example, when a swell component intersects the flight track at a large angle, a relatively low apparent frequency of encounter is produced. The filter must be designed in anticipation of this situation. In doing so, some aircraft motion will remain as part of the data. This can be significant when the aircraft is flying within the marine boundary layer during turbulent wind conditions.

In the present study a Martin filter (Martin, 1959) was used and its design for this application is discussed by McClain and Walden (1979). This filter incorporates the properties of zero phase shift and adjustable cut-off and response-function slope. The steepness of the response function is compromised by overshoot (Gibbs phenomena). The filter is shown in Fig. 4.1. A digitization rate of 45 Hz was used which for these flights yielded a sample spacing of between 2 and 3 m. In order to remove any aircraft motion that managed to pass through the filter, accelerometer data were used. The procedure in handling vertical acceleration was to 1) remove the mean

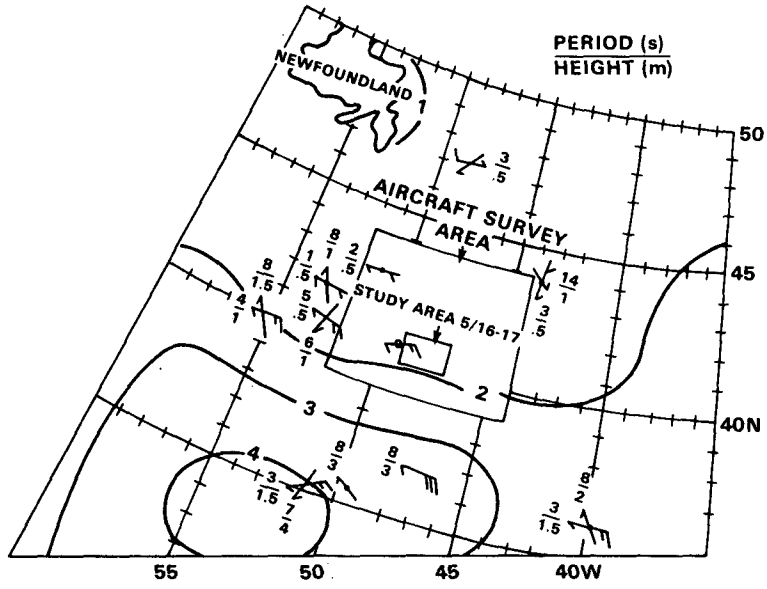

FIG. 3.6. Canadian METOC analysis of sea state at 1200 GMT 17 May 1979.

value so as to minimize parabolic trends produced by double integration, 2) double-integrate the resultant acceleration, 3) filter both the profilometer and aircraft-displacement time series, and 4) subtract the profilometer record from the residual aircraft displacement since the profilometer measures the inverted surface.

This procedure has previously been quite success-

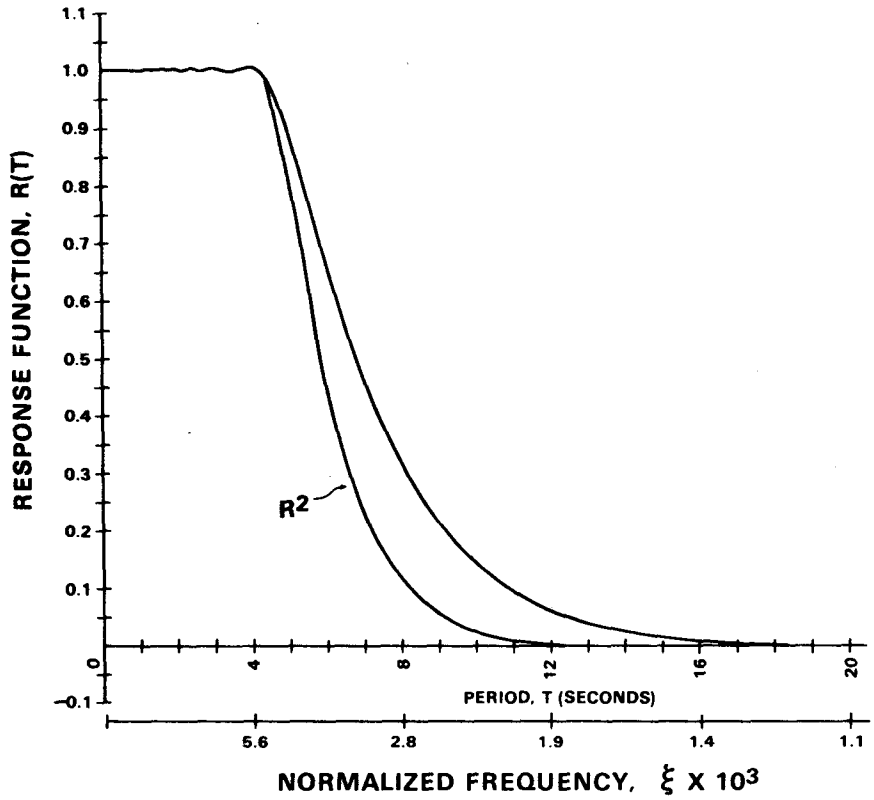

FIG. 4.1. Martin high-pass filter frequency-response function. The frequency is normalized by the sampling frequency, 45 Hz.

fully applied on a high-sea-state data set to derive power spectra and skewness (McClain *et al.*, 1982). It is a modification of an earlier procedure using frequency-domain processing described by McClain *et al.* (1980). A test of the analysis is the correlation between values along sections of different tracks that are located in similar positions with respect to the front. These results are given in the following section.

For single-track patterns, the incorporation of the wave-motion correction is often necessary when the ground speed of the platform is substantially reduced by high winds, and the longer wavelength components' phase speeds can be a significant fraction of the ground speed. In the present analysis, the graphic method is used and the phase speed correction is dropped, θ is assigned a value of zero, and (2.17) becomes $\hat{k} = k$.

Since the wave field is complex and therefore noisy, coarse resolution transforms of 512 points are used in order to obtain smoother spectra through averaging, to increase statistical confidence, and to make recognition of spectral peaks easier. The number of spectra averaged varied with location, but the mean number was eight. The Blackman-Harris 4-point window function was applied to the time series of each transform (Harris, 1978).

5. Results and discussions

As stated earlier, the objectives of this experiment were two-fold. The first was to study the feasibility of determinating wave-propagation directions in a complicated sea state from multi-track profilometer data. The second was to measure the effect of wave-current interactions across strong oceanic fronts. The significant wave height and the skewness values along each flight track are given in Fig. 5.1. In order to have tightly grouped tracks for determining the directions

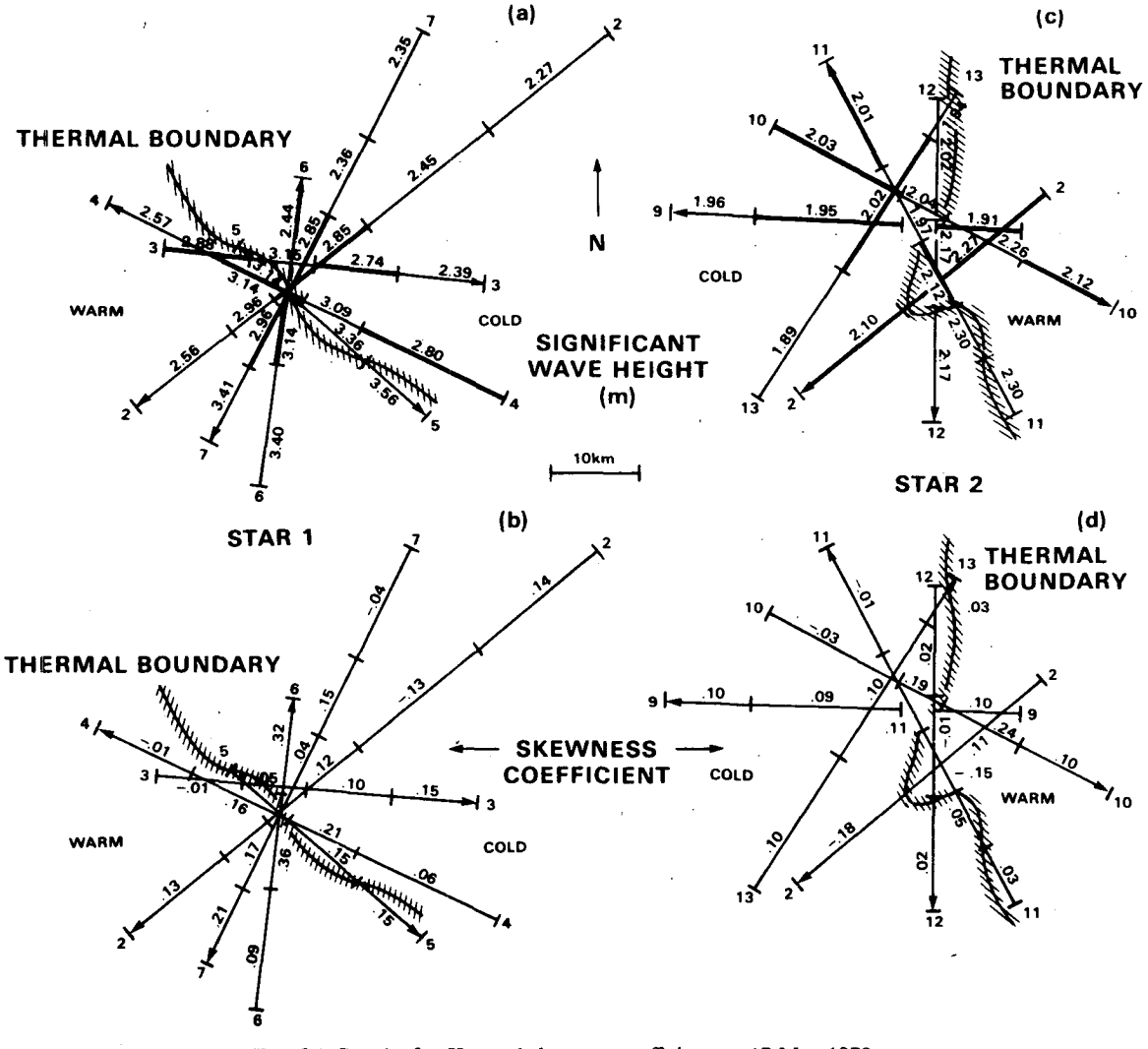

FIG. 5.1. Results for $H_{1/3}$ and skewness coefficient on 17 May 1979.

of wave propagation, only the spectra from the sections near the front are used. These sections are indicated by heavier lines. The results of our studies are presented separately in the following sections.

a. Determination of wave-system directions

Each star pattern is further divided into two subgroups using the temperature boundary as the dividing line. This division is essential because across the frontal line there are strong current and SST changes that could alter the wave condition. The designations are S_{ab} where a is the star number, b the subpattern number, and $b = 1$ is the cold-water side of the front.

Take the pattern S_{11} as an example. First, the apparent wavenumber spectra along different flight tracks are presented in Fig. 5.2 and are arranged in counterclockwise order. The shapes of the spectra show such a high degree of variation that little resemblance can be detected. Since track 5 lies athwart the frontal boundary, it is not included in the analysis for the wave-direction determination, but is used as a check after the direction is determined. The spectra can be roughly divided into three basic types. The first type shows a single peak as in spectra a and d. The second type is more representative. All the spectra in this group show two distinct peaks as in spectra b, e and f. The third type shows multiple peaks as in spectrum c. Careful examination of spectrum d shows

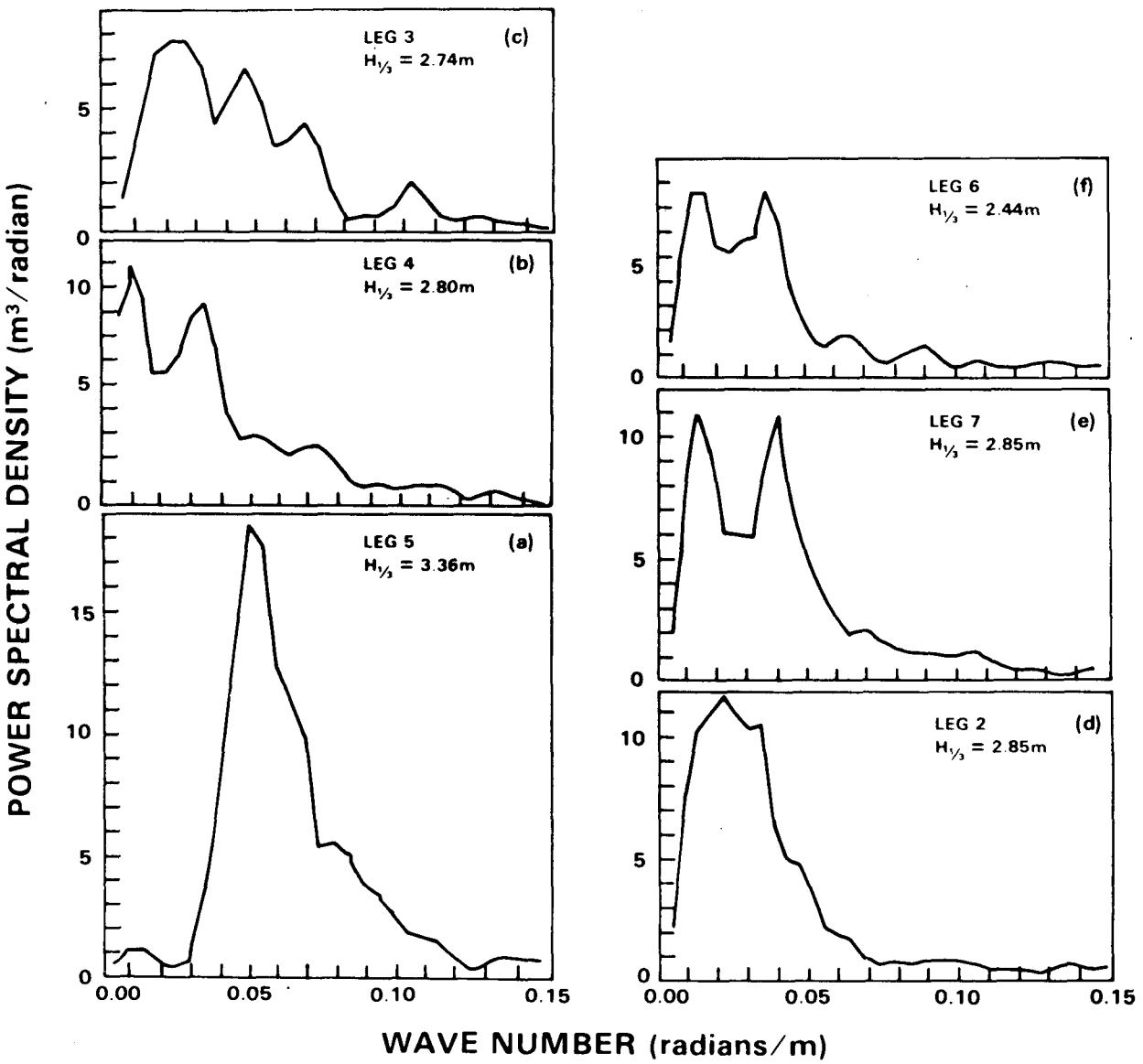

FIG. 5.2. Apparent wavenumber spectra for pattern S_{11}.

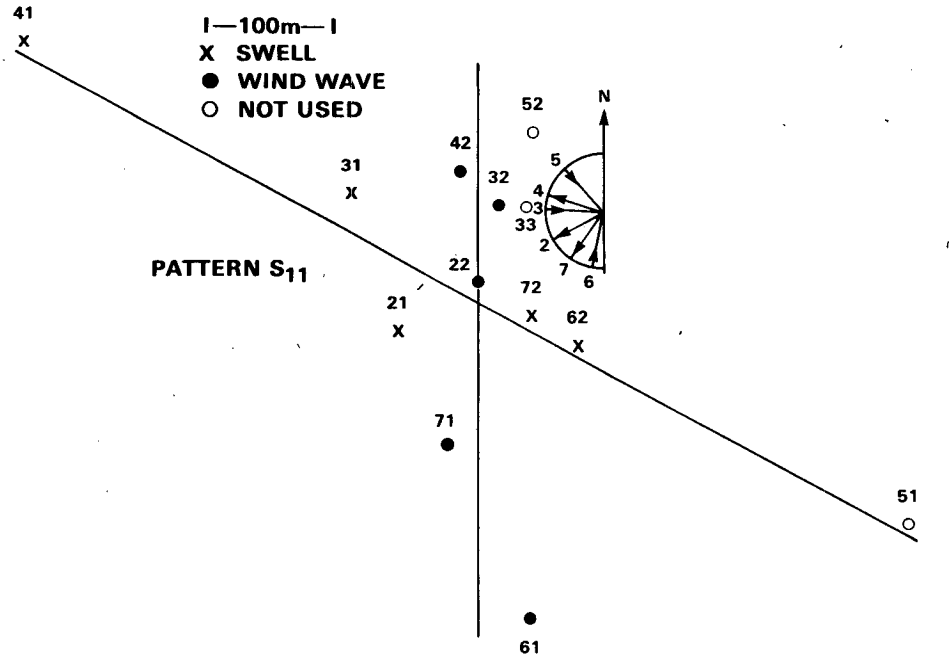

FIG. 5.3. Determination of dominant wavelengths for pattern S_{11}.

the possibility of two peaks that almost merge. Since most spectra show two prominent peaks, it was decided to limit our search to a two-wave-system field.

The apparent wavelengths of all the peaks are calculated and plotted in Fig. 5.3 according to the method discussed in Section 2. The directions of the flight tracks are shown in a semicircle centered at the origin. All the points are plotted within a 180° half-plane. Each terminal point of the wavelength is labeled by a two digit number, *mn*. The first digit identifies the track number and the second number is the peak number in the order of decreasing wavelength. Examination of the distribution of points suggests two distinct lines. The first one consists of the points 41, 31, 21, 72 and 62. A least-squares fit of a straight line gives a correlation coefficient of 0.94. The second line consists of 42, 32, 22, 71 and 61. These straight lines are treated as the crest-lines of the swell and the dominant wind-wave component, respectively. Table 5.1 provides the results from the four subpatterns.

Several fine points should be clarified. First, there is a considerable amount of judgment used in selecting the points for a particular line-fitting. For example, the group of 31, 21, 71 and 61 could be a strong candidate. However, if such a line were chosen, the point 41 would have to be left out. From Fig. 5.2b, 41 represents a rather strong peak, and omission of it would be unreasonable. As a check of the final choice, data from flight track 5 were used. From spectrum 5.2a, three peaks are identified, even though the spectrum is dominated by one peak. Point 51 falls right on the swell crest-line and 52 falls reasonably close to the wind-wave crest.

The staggering of the points relative to the best-fitted line also contains information. Take the wind-wave crest-line for example. All the points (42, 22, 71) showing longer wavelengths are from flight tracks moving to the west. All the points (52, 32, 61) showing shorter wavelength are from the flight tracks moving to the east. This pattern suggests that the wind

TABLE 5.1. Summary of wave systems data.

	Wind waves			Swell			
Pattern	Length (m)	Direction (deg)	Correlation coefficient	Length (m)	Direction (deg)	Correlation coefficient	INS Wind [heading (deg)/ speed (m s^{-1})]
S_{22}	160	291	0.66	205	224	0.93	285/8.5
S_{21}	135	281	0.80	188	232	0.87	275/8.5 265/10
S_{11}	157	270	—	180	208	0.89	259/12.5
S_{12}	111	255	0.95	205	232	0.77	263/12.5

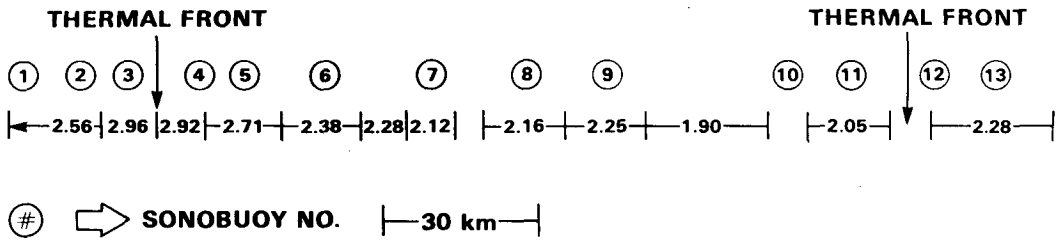

FIG. 5.4. Significant wave height (m) variability along track 2.

waves are propagating to the west, roughly parallel to the local wind. This method of determining the direction failed to give consistent answers for the swell in this case. Only patterns S_{11} and S_{22} gave clear indications that the swell was moving to the SW, while S_{21} was ambiguous and S_{12} indicated a NE direction.

A simple technique that can offer an unambiguous answer to the direction of wave propagation is flying the same track in opposite directions. The difference in locations of the peaks will be doubled and therefore easier to detect. There are points such as 33, which were not used in the crest-line fitting. These points suggest the existence of additional wave systems as indicated in Fig. 3.6. The available data cannot offer a consistent explanation. Wave-rider data would be needed to separate these systems clearly.

b. Variations of the waves: Wave-current interactions

Based on the results summarized in Figs. 5.1a–5.1d and Table 5.1, general trends in the waves' variations can be detected. While it is true that the seas are higher at Star 1 than at Star 2, track 2 across the entire feature has a local minimum in $H_{1/3}$ of 1.90 m (Fig. 5.4). Unfortunately sonobuoy 9 failed. Since the winds were light, the wind waves would be expected to be nearly fully developed and fetch effects are not expected to cause significant changes across the feature. Note from Table 5.1 that the wind-wave direction follows the INS wind direction from track 2 quite closely at all locations.

Detailed examination of the significant wave height data along each flight track in Star 2 shows that there is no dramatic change in the significant wave height. The situation in Star 1 is quite different. The mean skewness values determined for each side (warm and cold) of each star pattern (track 5 excluded) indicate that in both cases the skewness is roughly 40% higher in the warm-water regime. One should be cautious about inferring too much from these skewness changes since there is considerable scatter in the individual values. To illustrate this change, the apparent wavenumber spectra along flight track 7 are shown in Fig. 5.5. All the spectra show two prominent peaks at approximately the same location, as expected, because they should have similar projections. From Fig. 5.3, it also is clear that the lower-wavenumber peak (hence the longer wavelength) on this projection actually represents the wind waves.

Along the track, the swell component's spectral density ranges in value from 6 to 11, but with no systematic change. The wind-wave component is very stable until the front is crossed where an enhancement in peak value of 1.5 times the preceding value is found. Track 5 is the best indicator of the true response since it is parallel to the front and therefore is a sample of more homogeneous seas. The fact that track-5 $H_{1/3}$ values are consistently high testifies to the fact that analysis of any transecting track results in lower values on account of smoothing or averaging inhomogeneous data. Along track 5, the peak enhancement is even greater than indicated in Fig. 5.5d. The same type of change as found in track 7 occurs along track 6. The westernmost segment of track 2 indicates a significant decrease in $H_{1/3}$ that appears to be inconsistent with tracks 6 and 7. No adequate explanation can be given. Visual observations of increasing frequency of white-capping across the boundary also support the results of the significant wave height and skewness changes. Since no significant change in the horizontal wind as recorded in the INS data (245 m above the surface) across the western frontal boundary was observed, two possibilities are advanced to explain these changes. Since a response in aircraft motion was detected in the accelerometer data indicating an increase in turbulence, the first possibility is due to the change of the air-sea boundary-layer structure. An increase in SST across the frontal boundary will cause the boundary layer to become unstable, thus intensifying turbulence and wave growth. For lack of detailed wind-wave generation theory, no quantitative prediction can be offered. There are, however, quantitative data indicating some difficulty in this explanation. According to this explanation, as the wave energy grows, the wavelength should also increase or at least remain the same. But the summary in Table 5.1 shows that the wavelength decreased from 157 to 111 m across the frontal boundary. This is by far the largest change in all the cases. This discrepancy compels us to investigate the second possibility, wave-current interactions.

The surface currents on the 17th are tabulated in Table 5.2 and are decomposed into along-front and

across-front components with positive v in the downstream direction and positive u to the right. Generally, the v-component dominates and the flow is essentially a shear current similar to that used by Longuet-Higgins and Stewart (1961). Since we measure directly the values of k and θ (the angle between the wave ray and the across-front axis) on each side of the front, a comparison between theory and measurement is possible. The expressions given by theory that can be most easily tested are for energy and wavenumber:

$$E_2/E_1 = \sin(2\theta_1)/\sin(2\theta_2), \tag{5.1}$$

$$k_2/k_1 = \sin\theta_1/\sin\theta_2 . \tag{5.2}$$

The subscripts 1 and 2 respresent initial and final values, respectively. In this case, for the wind waves at the western front, $\theta_1 = 48°$ and $\theta_2 = 33°$ which result in $E_2/E_1 = 1.09$ as compared to 1.5 seen in track 7. From (5.2), $k_2/k_1 = 1.36$ as compared to 1.41 from the graphic-method determination of wavelength. In the theoretical derivation, Eq. (5.2) is a consequence of the irrotationality assumption coupled with the constraint that all variables are independent of the along-front coordinate. The latter condition seems reasonable since the currents are fairly unidirectional, and the distance across the front is fairly small. However, since considerable wave-breaking is occurring and the boundary layer is changed, one would not expect (5.1) to be valid for the wind-wave field and (5.2) is only approximately satisfied.

Using the mean current velocity of stations 1 and 2 and applying the expression

$$\theta_2 = \sin^{-1}[\sin\theta_1/(1 - v_2 \sin\theta_1/c_1)^2], \tag{5.3}$$

where $c_1 = (g/k_1)^{1/2}$, $\lambda_1 = 157$ m, $\theta_1 = 48°$ and $v_2 = 1.50$ m s^{-1}, the predicted change in direction is 8°, but 15° was observed. If (5.3) is applied to the swell, the result implies that the swell should not respond since θ_1 is only 14°. However, the measured value of θ_2 is −10° indicating a 24° refraction northward into the current which is unlikely and renders (5.2) unusable. Therefore, this disagreement is probably due to uncertainty in the graphic method in finding θ_1 and θ_2 for the swell.

If we apply a similar procedure to the wave components at the eastern front where they are moving

TABLE 5.2. Decomposition of current components v and u (m s^{-1}).

Sono-buoy No.	V (m s^{-1})	Heading (deg)	θ'	Along-front v	Across-front u	
1	1.57	132	0	1.57	0	
2	1.44	132	0	1.44	0	
3	0.93	143	−11	0.91	0.18	Western front
4	1.09	123	9	1.08	−0.17	
5	0.73	107	25	0.66	−0.31	
6	0.54	116	16	0.52	−0.15	
7	0.09	SE	—	—	—	
8	0.30	75	—	—	—	
10	0.73	19	8	0.72	0.10	
11	0.80	3	−8	0.79	−0.11	Eastern front
12	1.07	0	−11	1.05	−0.20	
14	0.55	25	+14	0.53	0.13	
15	1.46	10	−1	1.46	0	

θ' is the angle between the current vector and the front.

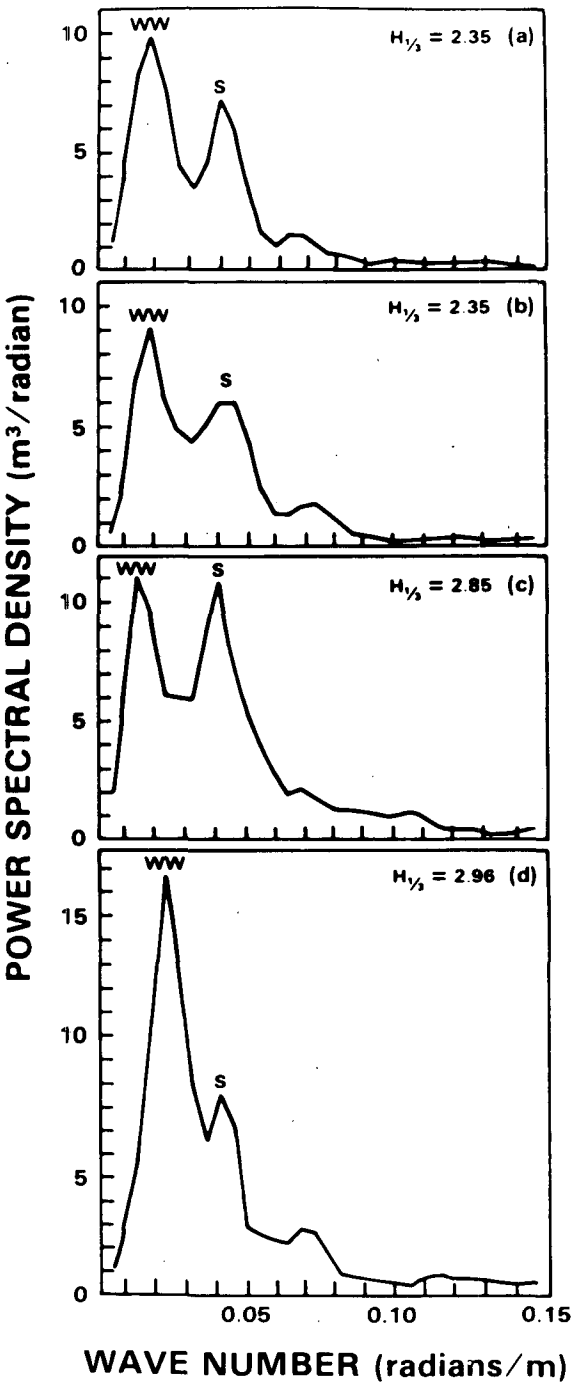

FIG. 5.5. Spectral variability along track 7.

from higher to lower velocity water, we see that the wind waves are initially propagating nearly perpendicularly to the current direction (the mean direction for stations 10–15), but have a component in its direction. The refraction across the front is to the south by 12°, which is against the current, as expected, and with the change in wind direction. However, solving (5.2) and (5.3) for θ_2 results in very small predicted changes. No change in the wind-wave height is predicted. The swell offers a better comparison since it is traveling at a respectable angle to the current. Here $\theta_1 = 57°$ and $\theta_2 = 49°$, as measured. Application of (5.2) to each side results in $\sin(\theta/\lambda)$ equaling 0.00409 on the east and 0.00401 on the west. Using (5.3) with $\theta_1 = 57°$ and $v_2 = 0.92$ m s^{-1} (mean for sonobuoys 11 and 12), $\theta_2 = 50°$ in excellent agreement with the measured value of 49°. The change in $H_{1/3}$ can be computed by taking the square root of (5.1) which results in a value of 0.96 for the swell. Using the $H_{1/3}$ values corresponding to the segments used in determining the θ's, the ratio of the mean values from each subpattern is also 0.96. Therefore, the change in sea state at the eastern front is due to swell modification by the currents. In this last situation, the theoretical assumptions are satisfied and the predictions are corroborated by the measurements.

6. Conclusions

This experiment was designed with two objectives in mind. The first one was to investigate the feasibility of using profilometer data to determine the directional properties of a wave field that contains more than the simple downwind component. The second objective was to study the quantitative effects of the wave-current interactions. Based on these results, the following conclusions can be made:

1) The profilometer can be used to determine the directional properties of the wave field. The accuracy of the direction of wave propagation is better than ±10° and the wavelength for each dominant component can be determined to within 10%. It is suggested that future profilometer-data collection should be executed with more than just one flight track upwind or downwind. Multitrack data are not only more informative but also offer cross-checks which make the results more reliable.

2) The presently available wave-current interaction theories offer good quantitative results when all the assumptions are satisfied. The influence of changes in air-sea boundary-layer structure across the oceanic fronts plays an important role in wave modification. Further studies of both interactions are needed. Profilometer data can play an indispensible role in the studies because of the spatial coverage they can provide. This particular study was hampered somewhat by the fact that *in situ* data from a wave-rider buoy, observations of wave direction, air-sea temperature differences and surface wind speeds were not available as originally planned. Also, navigational errors compromised the current estimates somewhat on the 17th. Future studies of this nature must incorporate all of these measurements.

Acknowledgments. The authors would like to thank W. D. Hart for his assistance in developing the algorithm and software used in the profilometer analysis, A. Gault for digitizing the data, H. Walden for helping in the Martin filter design, and J. Kerling for his assistance during the P-3 flights. Also, we wish to thank the reviewer who brought the existing work of R. B. Long to our attention and who made some valuable comments. The analysis of this data set was supported by NASA RTOP 146-40-15.

REFERENCES

Barber, N. F., 1949: The behavior of waves on tidal streams. *Proc. Roy. Soc. London*, **A198**, 81–93.

Barnett, T. P., and J. C. Wilkerson, 1967: On the generation of ocean wind waves as inferred from airborne radar measurements of fetch-limited spectra. *J. Mar. Res.*, **25**, 292–328.

Bowden, K. F., 1948: Some observations of waves and other fluctuations in a tidal current. *Proc. Roy. Soc. London*, **A197**, 403–425.

Charnock, H., 1981: Air-sea interaction. *Evolution of Physical Oceanography*, B. A. Warren and C. Wunsch, Eds., MIT Press, 482–503.

Clarke, R. A., R. F. Reininger and B. A. Warren, 1980: Current system south and east of the Grand Banks of Newfoundland, *J. Phys. Oceanogr.*, **10**, 25–65.

Fu, L.-L., and B. Holt, 1982: Seasat views oceans and sea ice with synthetic aperture radar. JPL Publ. 81-120, Jet Propulsion Laboratory, 200 pp.

Hammond, D. L., and C. R. McClain, 1980: Spectral distortion inherent in airborne profilometer measurements of ocean wave heights, *Ocean Eng.*, **7**, 99–108.

Harris, F. J., 1978: On the use of windows for harmonic analysis with the discrete Fourier transform. *Proc. IEEE*, **66**, 51–83.

Hayes, J. G., 1980: Ocean current wave interaction study. *J. Geophys. Res.*, **85**, 5025–5031.

Huang, N. E., D. T. Chen, C. C. Tung and J. R. Smith, 1972: Interactions between steady non-uniform currents and gravity waves with applications for current measurements. *J. Phys. Oceanogr.*, **2**, 420–431.

Jackson, F. C., W. T. Walton and P. L. Baker, 1982: Directional spectra from air- and spaceborne radar. *Directional Wave Spectra Applications*, R. L. Wiegel, Ed., ASCE, 299–314.

Jones, D. R., 1953: Note on observed vertical wind shear at low levels over the ocean, *Bull. Amer. Meteor. Soc.*, **34**, 393–396.

Kats, A. V., and I. S. Spevak, 1980: Reconstruction of the sea-wave spectra from the measurements of moving sensors. *Izv. Atmos. Ocean. Phys.*, **16**, 194–200.

Kenyon, K. E., 1971: Wave refraction in ocean currents. *Deep-Sea Res.*, **18**, 1023–1034.

Kondo, J., 1975: Air-sea bulk transfer coefficients in diabatic conditions. *Bound.-Layer Meteor.*, **9**, 91–112.

LaViolette, P. E., 1981: Variations in the frontal structure of the southeastern Grand Banks. NORDA Tech. Note No. 87, 48 pp.

——, S. Petherych and J. F. R. Gower, 1980: Oceanographic implications of features in NOAA satellite visible imagery. *Bound.-Layer Meteor.*, **18**, 159–176.

Liu, P. C., and D. B. Ross, 1980: Airborne measurements of wave growth for stable and unstable atmospheres in Lake Michigan, *J. Phys. Oceanogr.*, **10,** 1842–1853.

Long, R. B., 1979: On surface gravity wave spectra observed in a moving frame of reference. NOAA Tech. Memo. ERL AOML-38, 34 pp.

Longuet-Higgins, M. S., and R. W. Stewart, 1960: Changes in the form of short gravity waves on long waves and tidal currents. *J. Fluid Mech.*, **8,** 565–583.

——, and ——, 1961: The changes in amplitude of short gravity waves on steady non-uniform currents. *J. Fluid Mech.*, **10,** 529–549.

——, and ——, 1964: Radiation stresses in water waves: A physical discussion, with applications. *Deep-Sea Res.*, **11,** 529–562.

Martin, M. A., 1959: Frequency domain applications in data processing. *IRE Trans. Space Electron. Telemetry*, March, 33–41.

McClain, C. R., and H. Walden, 1979: On the performance of the Martin digital filter for high- and low-pass applications. NASA Tech. Memo. No. 80593, 24 pp.

——, D. T. Chen and D. L. Hammond, 1979: Comments on "GEOS-3 wave height measurements: An assessment during high sea state conditions in the North Atlantic" by C. L. Parsons. *J. Geophys. Res.*, **84,** 4027–4028.

——, —— and ——, 1980: Gulf Stream ground truth Project: Results of the NRL airborne sensors. *Ocean Eng.*, **7,** 55–97.

——, —— and W. Hart, 1982: On the use of laser profilometry for ocean wave studies. *J. Geophys. Res.* (in press).

Ross, D. B., V. J. Cardone and J. W. Conaway, Jr., 1970: Laser and microwave observations of sea-surface conditions for fetch-limited 17- to 25-m/s winds. *IEEE Trans. Geosci. Electron.*, **GE-8,** 326–336.

Schule, J. J., Jr., L. S. Simpson and P. S. DeLeonibus, 1971: A study of fetch-limited wave spectra with an airborne laser. *J. Geophys. Res.*, **76,** 4160–4171.

Sugimori, Y., 1973: Dispersion of the directional spectrum of short gravity waves in the Kuroshio Current. *Deep-Sea Res.*, **20,** 747–756.

Sweet, W., R. Fett, J. Kerling and P. E. LaViolette, 1981: Air-sea interaction effects in the lower troposphere along the north wall of the Gulf Stream. *Mon. Wea. Rev.*, **109,** 1042–1052.